Physics of Plasmas ARTICLE scitation.org/journal/php

Verification of an energetic-electron-driven β-induced Alfvén eigenmode in the HL-2A tokamak

Cite as: Phys. Plasmas **26**, 102507 (2019); doi: 10.1063/1.5115811
Submitted: 22 June 2019 · Accepted: 20 September 2019 ·
Published Online: 17 October 2019

Yang Chen,[1,2,3] Wenlu Zhang,[1,2,3,4,5,a)] Junyi Cheng,[1,2,3] Zhihong Lin,[4,6] Chao Dong,[2,3] and Ding Li[1,2,3]

AFFILIATIONS

[1]School of Physical Sciences, University of Science and Technology of China, Hefei, Anhui 230026, China
[2]Beijing National Laboratory for Condensed Matter Physics and CAS Key Laboratory of Soft Matter Physics, Institute of Physics, Chinese Academy of Sciences, Beijing 100190, China
[3]School of Physical Sciences, Beijing 100049, China
[4]Department of Physics and Astronomy, University of California, Irvine, California 92697, USA
[5]Songshan Lake Materials Laboratory, Dongguan, Guangdong 523808, China
[6]Fusion Simulation Center, Peking University, Beijing 100871, China

[a)]**Electronic mail:** wzhang@iphy.ac.cn. URL: https://www.indac.info.

ABSTRACT

An energetic-electron-driven β-induced Alfvén eigenmode (e-BAE) in an HL-2A tokamak experiment (discharge #17461) was studied using a gyrokinetic particle simulation code. Investigations of e-BAEs excited by an initial perturbation, an external antenna, and an energetic-electron pressure gradient were performed, and the measured eigenfrequencies were found to be close to the experimental observations and the theoretical predictions. The damping mechanism is also discussed based on the simulation results. The e-BAE becomes unstable when the driving force of the energetic-electron pressure gradient exceeds the total background damping. Simulations show that the e-BAE propagates along the diamagnetic direction of the energetic electrons and that the most unstable mode number is $n/m = 1/3$; these findings are in good agreement with the experimental observations. The simulation results also show that the mode is radially localized near the rational surface. Both the mode width and growth rate increase as the background plasma density increases. As the density and temperature of the energetic electrons increase, the eigenfrequency increases slightly, and the growth rate increases considerably.

I. INTRODUCTION

In fusion plasmas, such as that in the International Thermonuclear Experimental Reactor (ITER),[1] the confinement of energetic particles has always been of great concern. These particles can drive various Alfvén instabilities,[3] such as toroidal Alfvén eigenmodes (TAEs),[2] reversed shear Alfvén eigenmodes (RSAEs),[3] β-induced Alfvén eigenmodes (BAEs), and β-induced Alfvén acoustic eigenmodes (BAAEs), which can induce the loss of energetic particles and cause their confinement to degrade.

A BAE arises due to the finite compressibility induced by the geodesic curvature of the equilibrium magnetic field, together with the plasma pressure.[4,5] Its eigenfrequency is near the β-induced gap of the Alfvén continuum in a toroidal geometry,[4] which is close to the thermal ion transit frequency and the ratio of the sound speed to the major radius R_0; thus, a BAE is subject to resonant interactions with both thermal ions and energetic particles as well as acoustic waves.

Several theoretical explanations for the excitation of BAEs have been proposed, including discrete Alfvén eigenmodes (AEs),[6] kinetic ballooning modes (KBMs),[7] energetic particle modes (EPMs),[8–10] and hybrid modes between Alfvénic and KBM branches or between Alfvénic and ion acoustic branches.[11]

BAEs were first reported in DIII-D[12] with energetic ions induced by neutral beam injection (NBI) and in TFTR[13] with energetic ions. Additionally, they were observed in KSTAR[14] during neutral beam heating and in Tore Supra[15] during ion cyclotron resonance heating. BAEs arising during strong tearing mode (TM) activities have also been investigated in many experimental devices, such as in the FTU plasma without energetic ions,[16] in the LHD plasma during strong

interchange modes,[17] in EAST with low hybrid waves (LHWs),[18] and in TEXTOR with a low-density plasma.[19]

Energetic-ion-driven BAEs (i-BAEs) have been widely investigated by means of experimental observations, theoretical studies, and simulations. On the other hand, energetic electrons originating from Ohmic heating, electron cyclotron resonance heating (ECRH),[20,21] and alpha particle heating can also easily drive the formation of an energetic-electron-driven β-induced Alfvén eigenmode (e-BAE) through wave-particle interactions.

Recently, an e-BAE was identified in both Ohmic heating and ECRH for the first time[22] in the medium-sized HL-2A tokamak;[23] subsequently, the coexistence of e-BAEs in multiple modes was observed.[24]

Further analysis of e-BAEs[25] has confirmed that they can be identified by a generalized fishbonelike dispersion relation and magnetic-island-induced BAE dispersion. Observations of BAEs in J-TEXT[26] indicate that runaway electrons together with magnetic perturbations in cases of low-density discharge can excite BAEs in Ohmic plasmas. The experiment in EAST[16] has shown that increasing the population of energetic electrons may result in the excitation of BAEs. Recent theoretical developments[27] further predict that energetic particles preferentially excite the BAE branch rather than the ion-sound wave (ISW) branch.

Although many studies of e-BAEs have been conducted, both experimentally and theoretically, fewer simulations have been performed,[28,29] specifically simulations based on experimental equilibrium profiles.

In this work, we use the Gyrokinetic Toroidal Code (GTC)[30] to simulate the e-BAE in HL-2A discharge #17461,[24] in which the e-BAE is one of the most notable instabilities excited by energetic electrons.

GTC has been successfully applied to study various Alfvén eigenmodes, such as TAEs,[31–33] RSAEs,[34,35] and i-BAEs.[36,37] Linear and nonlinear e-BAE analyses have been carried out by Cheng *et al.*[28,29] The interaction between a BAAE and a BAE has been simulated by Liu.[38] Wang has simulated a discrete kinetic BAE (KBAE)[39] and a nonlinear i-BAE[40] using the hybrid magnetohydrodynamics (MHD) gyrokinetic code XHMGC.[41,42] A simulation based on the National Spherical Torus Experiment (NSTX) parameters[43] has been performed using the hybrid particle/MHD code M3D.[44] A BAE-like mode has been simulated based on the DIII-D parameters using the M3D-K code.[45] Even- and odd-parity KBAEs[46] have been simulated using a kinetic Alfvén eigenmode solver (KAES) based on a recently developed AMC code.[47]

In discharge #17461, the e-BAE was excited when ECRH was turned on and propagated in the diamagnetic direction of the energetic electrons. The electron temperature was measured via electron cyclotron emission (ECE), the ion temperature was measured via neutral particle analysis (NPA), and the electron density was measured with an eight-channel hydrogen cyanide (HCN) laser interferometer in the core region and microwave reflectometry at the edge. The e-BAE toroidal/poloidal number was measured through the phase analysis of Mirnov signals, and the mode frequency and mode position were measured through the analysis of soft X-rays (SXR). Here, we focus on simulating the mode with the toroidal/poloidal mode number $n/m = 1/3$, which starts as an e-BAE at approximately 575 ms and has a frequency of 19 kHz.

The paper is organized as follows. The physical model used in the e-BAE simulation is described in Sec. II. The simulation setup based on the experimental parameters is introduced in Sec. III. The antenna excitation setup and its results are described in Sec. IV A. The initial perturbation excitation setup and its results are presented in Sec. IV B. The energetic electron excitation setup and its results are reported in Sec. IV C. A summary of this work is given in Sec. V.

II. SIMULATION MODEL

For the use of the nonlinear gyrokinetic equations,[48] the adopted ordering is as follows:

$$\frac{\omega}{\Omega} \sim \frac{k_{\|}}{k_{\perp}} \sim \frac{\delta B}{B_0} \sim \frac{e\delta\phi}{T} \sim O(\epsilon), \tag{1}$$

where ω is the typical frequency, $k_{\|}$ and $k_{\perp}$ are the parallel and perpendicular wave numbers, respectively, of the instability, Ω is the ion cyclotron frequency, δB is the perturbed magnetic field, B_0 is the equilibrium magnetic field, $\delta\phi$ is the perturbed electrostatic potential, and T is the plasma temperature.

The nonlinear Vlasov equations are used to describe the thermal ions in this GTC simulation,

$$\left(\frac{\partial}{\partial t} + \dot{\mathbf{X}}\cdot\nabla + \dot{v}_{\|}\frac{\partial}{\partial v_{\|}} - \mathcal{C}_i\right) f_i(\mathbf{X}, \mu, v_{\|}, t) = 0, \tag{2}$$

$$\dot{\mathbf{X}} = v_{\|}\frac{\mathbf{B}}{B_0} + \mathbf{v}_E + \mathbf{v}_c + \mathbf{v}_g, \tag{3}$$

$$\dot{v}_{\|} = -\frac{1}{m_i}\frac{\mathbf{B}^*}{B_0}\cdot(\mu\nabla B_0 + Z_i\nabla\delta\phi) - \frac{Z_i}{m_i c}\frac{\partial\delta A_{\|}}{\partial t}. \tag{4}$$

Here, $\mathbf{X}$ is the gyrocenter position, μ is the magnetic moment, $v_{\|}$ is the parallel velocity, and $\mathcal{C}_i$ is the collision operator. This equation is expressed in five-dimensional phase space for a system with a toroidal geometry. The index i denotes thermal ions, Z_i is the ion charge, and m_i is the ion mass. $\delta\phi$ and $\delta A_{\|}$ are the electrostatic potential and the vector potential parallel to $\mathbf{B_0}$, respectively.

Here, $\mathbf{B} = \mathbf{B}_0 + \delta\mathbf{B}$, where $\mathbf{B_0}$ and $\delta\mathbf{B}$ are the equilibrium and perturbed parts, respectively, of the magnetic field. $\mathbf{B}^* = \mathbf{B}_0^* + \delta\mathbf{B}$, where $\mathbf{B}_0^* = \mathbf{B}_0 + (B_0 v_{\|}/\Omega_\alpha)\nabla\times\mathbf{b}_0$ and $\delta\mathbf{B} = \nabla\times(\delta A_{\|}\mathbf{b}_0)$. Here, Ω_α is the cyclotron frequency of species α.

The $\mathbf{E}\times\mathbf{B}$ drift $\mathbf{v}_E$, the magnetic curvature drift $\mathbf{v}_c$, and the grad-$\mathbf{B}$ drift $\mathbf{v}_g$ are given by

$$\mathbf{v}_E = \frac{c\mathbf{b}_0\times\nabla\delta\phi}{B_0}, \tag{5}$$

$$\mathbf{v}_c = \frac{v_{\|}^2}{\Omega_\alpha}\nabla\times\mathbf{b}_0, \tag{6}$$

$$\mathbf{v}_g = \frac{\mu}{m_\alpha\Omega_\alpha}\mathbf{b}_0\times\nabla\mathbf{B}_0. \tag{7}$$

For energetic electrons, the Larmor radius is much smaller than that of thermal ions; meanwhile, the Larmor radius of thermal ions is of the same order as the characteristic spatial BAE scale. Therefore, the drift-kinetic model is adopted. Here, a subcycling method[28] is used in which the energetic electrons are pushed several times, while the ions and field quantities are updated once in each time step; this approach can save considerable computing time while maintaining good precision. For thermal electrons, the kinetic effect is much smaller than that for energetic electrons. Thus, the fluid-kinetic hybrid electron model[49] is

adopted to expand the electron response into a low-order adiabatic part and a high-order perturbation part with kinetic terms. In the lowest order of the fluid-kinetic hybrid model, the response of the adiabatic thermal electrons is described by the fluid continuity equation by integrating Eq. 2 in the drift-kinetic limit ($k_\perp \rho_e = 0$) in velocity space,

$$\frac{\partial \delta n_e}{\partial t} + \mathbf{B}_0 \cdot \nabla\left(\frac{n_{0e}\delta v_{\|e}}{B_0}\right) + \mathbf{B}_0 \mathbf{v}_E \cdot \nabla\left(\frac{n_{0e}}{B_0}\right) - \frac{1}{m_e \Omega_e}\mathbf{b}_0 \times \nabla\left(\delta P_{e\|} + \delta P_{e\perp}\right) \cdot \frac{\nabla B_0}{B_0} - n_{0e}\mathbf{v}_E \cdot \frac{\nabla B_0}{B_0} = 0, \quad (8)$$

where $\delta n_e = \int \delta f_e d\mathbf{v}$, $\delta P_{e\|} = \int m v_\|^2 \delta f_e d\mathbf{v}$ and $\delta P_{e\perp} = \int \mu B_0 \delta f_e d\mathbf{v}$. In a uniform plasma, according to Eqs. 19 and 20 of Ref. [49], $\delta P_{e\|} = \delta P_{e\perp} = e n_{0e} \delta \phi_{eff}$ to the lowest order. Here, n_{0e} is the electron density, and $\delta\phi_{eff}$ is the effective potential that represents the parallel electric field, $\delta E_\| = -\mathbf{b}_0 \cdot \nabla \delta \phi_{eff}$.

The system is closed, with the parallel Ampère law,

$$e n_{0e} \delta u_{\|e} = \frac{c}{4\pi}\nabla_\perp^2 \delta A_\| + Z_i n_{0i} \delta u_{\|i} - e n_{0fe} \delta u_{\|fe}, \quad (9)$$

and the gyrokinetic Poisson equations,

$$\frac{Z_i^2 n_i}{T_i}(\delta\phi - \delta\tilde{\phi}) = \sum_{\alpha=e,i,fe} Z_\alpha \delta n_\alpha. \quad (10)$$

Here, $\delta\tilde{\phi} = \sum_k \delta\phi_k \Gamma_0(k_\perp^2 \rho_i^2)$ is the second gyrophase-averaged electrostatic potential.[50]

Now, we will show that with kinetic effects turned off, the ideal MHD result is recovered from the gyrokinetic formulations. In the long-wavelength limit, $\delta E_\| = 0$ and $\nabla \times \mathbf{B}_0 \approx 0$, and Eq. (10) becomes

$$\nabla_\perp \cdot \left(\frac{\nabla_\perp \delta\phi}{v_A^2}\right) = -\frac{4\pi}{c^2}\left(Z_i \delta n_i - Z_e \delta n_e - Z_{fe}\delta n_{fe}\right). \quad (11)$$

Here, $v_A = B/\sqrt{4\pi n_i m_i}$ is the Alfvén velocity. By using Eq. (8) for all species, Eq. (9), and the charge neutrality condition $\sum_\alpha Z_\alpha n_{0\alpha} = 0$, we can obtain

$$\omega^2 \nabla_\perp \cdot \left(\frac{\nabla_\perp \delta\phi}{v_A^2}\right) - i\omega \frac{4\pi}{c}\nabla \cdot \left(\frac{\mathbf{b}_0}{B_0} \times \nabla \delta P\right) - \mathbf{B}_0 \cdot \nabla\left[\frac{1}{B_0}\nabla^2(\mathbf{b}_0 \cdot \nabla\delta\phi)\right] = 0, \quad (12)$$

with $\delta P = \delta P_i + \delta P_e + \delta P_{fe}$. Equation (12) recovers the ideal MHD equations.[39]

Finally, we derive the BAE linear dispersion relation by considering only the fluid electron pressure for simplicity. In a toroidal geometry, if we consider only a frequency ω and the toroidal/poloidal (n/m) harmonic, then the perturbed quantities of the Alfvén wave can be expressed as follows:

$$\delta\phi(r,\theta,\zeta,t) = \delta\hat{\phi}(r)\exp[i(n\zeta - m\theta - \omega t)]. \quad (13)$$

For a uniform plasma, the perturbed diamagnetic flow can be neglected in Eq. (8). The $v_\|$ term is dropped because $k_\| = 0$ for the BAE in the vicinity of the rational surface. Thus, Eq. (8) reduces to

$$\frac{\partial \delta n_e}{\partial t} = -n_{0e}\nabla \cdot \frac{c\nabla\delta\phi \times \mathbf{B}_0}{B_0^2}. \quad (14)$$

Using $\delta P_e = \delta n_e T_e = e n_{0e}\phi_{eff}$ and Eq. (14), the pressure term in Eq. (12) can be written as

$$-\frac{\partial}{\partial t}\frac{4\pi}{c}\nabla \cdot \left(\frac{\mathbf{b}_0}{B_0} \times \nabla \delta P_e\right) = -n_{0e}T_e \nabla\left(\nabla\delta\hat{\phi} \cdot \nabla \times \frac{\mathbf{B}_0}{B_0^2}\right) \cdot \nabla \times \frac{\mathbf{B}_0}{B_0^2}. \quad (15)$$

When terms of order $O(\epsilon^2/q^2)$ are dropped and flux averaging is performed, Eq. (12) becomes

$$\frac{1}{r}\frac{d}{dr} r\left(\frac{\omega^2}{v_A^2} - k_\|^2 - \frac{2C_s^2}{v_A^2 R_0^2}\right)\frac{d}{dr}\delta\hat{\phi} - \frac{m^2}{r^2}\left(\frac{\omega^2}{v_A^2} - k_\|^2 - \frac{2C_s^2}{v_A^2 R_0^2}\right)\delta\hat{\phi} - \frac{k_\|}{r}\frac{d(k_\| r)}{dr}\delta\hat{\phi} = 0. \quad (16)$$

Here, $C_s^2 = T_e/m_i$, and $k_\| = (n - m/q)/R_0$. When $k_\| = 0$, the Alfvén continuum reaches the accumulation point, $\omega^2 = 2C_s^2/R_0^2$.

More generally, the pressure term includes the kinetic ion pressure and the electron pressure, and the accumulation point frequency is given by

$$\omega_{\mathrm{CAP}} = \sqrt{\left(\frac{7}{2}T_i + 2T_e\right)/(m_i R_0^2)}. \quad (17)$$

Detailed derivations for the BAE frequency can be found in Refs. 5 and 51.

III. SIMULATION SETUP

The HL-2A tokamak has a circular cross section in the poloidal direction, and Fig. 1 shows the flux surface of discharge #17461 at 575 ms. Using the general geometric features of HL-2A and GTC, we can build the equilibrium geometry, including the field magnitude, the flux surface structure, the q-profile, and other profiles, including the radial temperature and density profiles of thermal ions and electrons, in a manner that is fully self-consistent with the experimental conditions. The major radius on the magnetic axis is $R_0 = 165$ cm, which is approximately 340 times the on-axis ion gyroradius ρ_{i0}. The on-axis magnetic field amplitude is $B_0 = 1.33$ T. The safety factor profile is given by $q = q(r)$ from the Tokamak Simulation Code (TSC), where r is the radial position with a minor radius of $a = 40$ cm.

In the large-aspect-ratio approximation, the poloidal flux is $\Psi_p(r) = B_0 \int_0^a r' q(r')\, dr'$.[52] On this basis, the relationship among q, r, and ρ can be formulated, where ρ is the square root of the normalized poloidal flux, $\rho = \sqrt{\Psi_p/\Psi_{pw}}$; here, Ψ_p is the poloidal flux, and Ψ_{pw} is the poloidal flux at the outermost flux surface.

After the above process, the radial position r is converted into the GTC basic radial coordinate ρ. The radial safety factor profile $q = q(\rho)$ is shown in Fig. 2(a), where the dashed lines indicate our simulation region in the radial direction, $0.696 \leqslant \rho \leqslant 0.952$, and the plus sign indicates the diagnosis point where the mode most likely exists, namely, the $q = 3$ rational surface located at $\rho = 0.83$.

The background ions are deuterium nuclei. The density of the thermal electrons and the temperature of the thermal particles

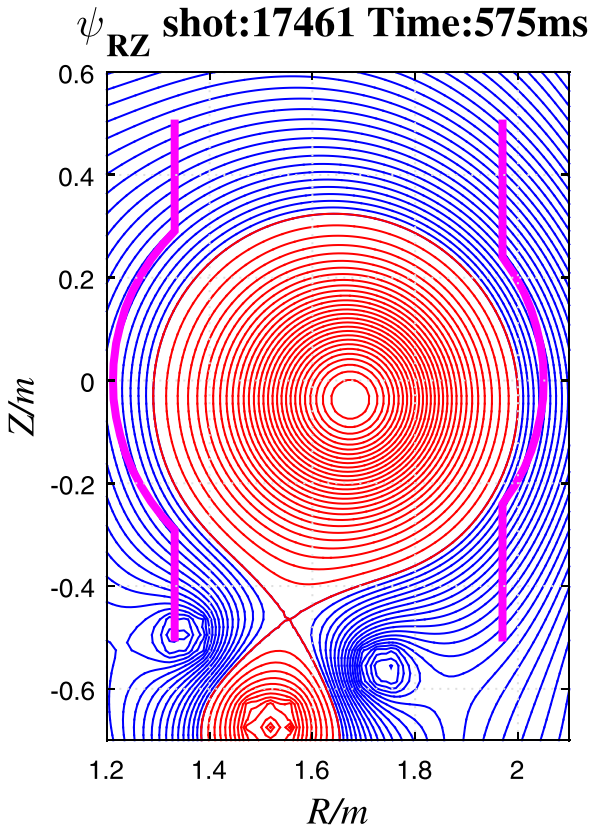

FIG. 1. Flux surface of HL-2A discharge #17461 at 575 ms. The tokamak has a circular cross section in the poloidal direction. The on-axis magnetic field is $B_{\psi 0} = 1.3$ T.

obtained from the experimental parameters are not plotted near the magnetic axis. Experimentally, from $\rho = 0.4$ to $\rho = 1.0$, the distributions of the electron density n_e, the thermal ion temperature T_i, and the thermal electron temperature T_e are as shown in Fig. 2(b).

In the simulations, the density profile used for the thermal electrons is a realistic profile obtained from the experimental parameters, and the thermal ion density n_i is obtained from the quasineutral condition $Z_i n_{0i} = n_0 + n_{fe}$ for a thermal ion charge number of $Z_i = 1$. Regarding the temperature profile of the thermal particles, we adopt an approximation in which only the temperature gradient of the energetic electrons is retained as the driving source, while the temperature gradient of the thermal particles is set to zero, i.e., the temperature profile is uniform. This approximation is adopted to separate the BAE from the mode driven by the thermal particle temperature gradient, and it is reasonable because the BAE is localized near the rational surface. At the $q = 3$ rational surface, where the e-BAE is most likely to exist, the thermal particle temperatures adopted here are $T_e = 0.3$ keV and $T_i = 0.025$ keV, with $\beta = 8\pi P/B_0^2 = 0.0003314$, where β is the ratio of the plasma thermal pressure to the magnetic pressure. To avoid high-frequency noise, we use a toroidal/poloidal filter to preserve only the $n/m = 1/(2, 3, 4)$ harmonics, while the other harmonics are neglected. According to Eq. (17), the Alfvén accumulation point frequency is $\omega_{\mathrm{CAP}} = \sqrt{(7T_i + 4T_e)/2m_i R_0^2} \approx 1.515 C_s/R_0$, with the sound speed being $C_s = \sqrt{T_e/m_i}$, and $f_{\mathrm{CAP}} = \omega_{\mathrm{CAP}}/2\pi = 18.3$ kHz.

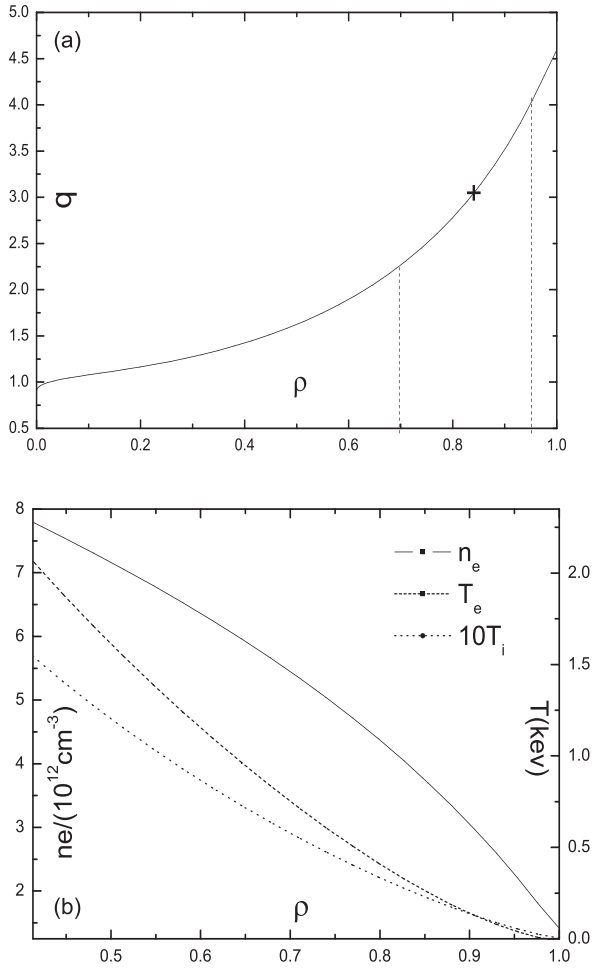

FIG. 2. Radial profiles of (a) the safety factor q, where the dashed lines indicate the simulation region in the radial direction and the plus sign indicates the diagnosis point and (b) the thermal electron density n_e, the thermal electron temperature T_e and the thermal ion temperature $10T_i$.

The numerical parameters have been carefully set based on convergence tests. The time step is $\Delta t = 0.01 C_s/R_0$. The poloidal wave vector is $k_\theta = m/r = 9.03$, and $k_\theta \rho_{i0} = 0.0439$. In this work, there are 96 radial grid points, 1600 poloidal grid points, and 8 toroidal grid points in the real space, and there are 50 marked particles of each species in each grid cell.

IV. SIMULATION RESULTS

We use Fig. 3 to evaluate the differences between all of the following cases and the continuous spectrum. This figure was produced by an eigenvalue code called ALCON, which uses a poloidal-spectral method to numerically solve the ideal MHD Alfvén continuum equation.[35] Here, the vertical axis represents the real frequency measured in kHz, and the horizontal axis represents the radial coordinate ρ. The thick lines are the $n = 1$ toroidal harmonics of the Alfvén branches, and the thin lines are the acoustic branches. Figure 3(b) presents an enlarged view of the $n/m = 1/3$ mode in the figure above.

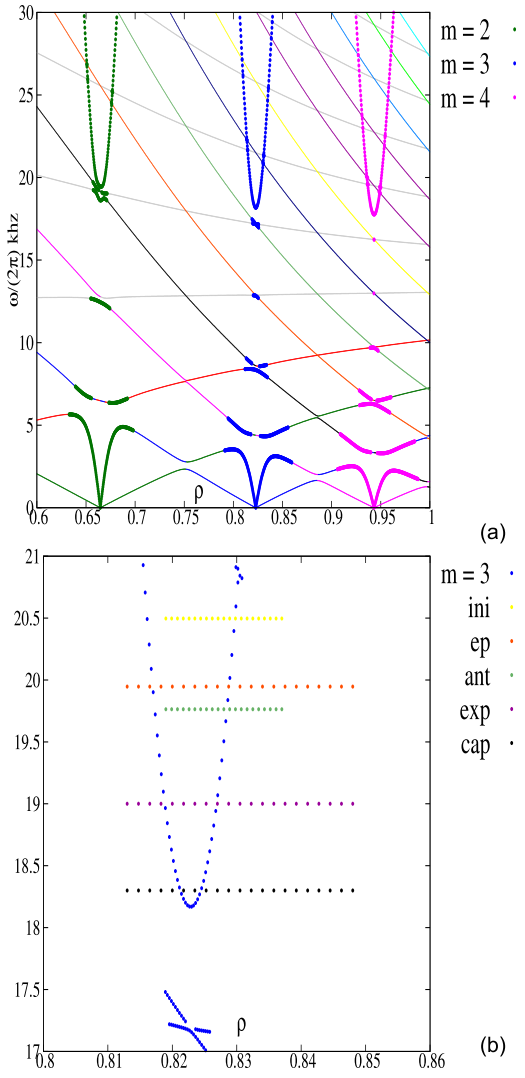

FIG. 3. (a) Alfvén continuous spectrum and acoustic spectrum for $n=1$ obtained using the eigenvalue code ALCON. (b) An enlarged partial view of the $n/m=1/3$ mode, in which the acoustic spectrum has been dropped. The straight lines individually correspond to the following three simulation cases, the experimental observation, and the accumulation point.

The five straight horizontal lines, from top to bottom, are the frequencies of the initial perturbation, the energetic electron excitation, the antenna excitation, the experimental observation, and the ideal MHD continuum accumulation point (CAP). The line lengths for the initial perturbation, energetic electron, and antenna excitation cases are each equivalent to the radial mode half-width for the corresponding case, while the line lengths for the accumulation point and the experimental observation have no practical meaning.

A. BAE excitation by an antenna

Now, let us consider the use of an external antenna[53] to excite an e-BAE. The antenna-driven method, which has been used in previous tokamak experiments,[54,55] allows us to measure the e-BAE frequency, damping rate, and propagation direction. The antenna excitation has the following form:

$$\delta\phi_{ant} = \delta\phi_{ant}(\psi)\cos(m\theta - n\zeta)\cos(\omega_{ant}t). \tag{18}$$

Here, $\delta\phi_{ant}(\psi)$ has a one-dimensional normal distribution that reaches its maximum at $\rho = 0.83a$, where the $q=3$ rational surface lies, and exponentially decays to zero at the edge of the simulation region.

The linear Vlasov equation is used to describe the thermal ions, the electrons are treated adiabatically, and the energetic electron component is dropped. According to induced cavity resonance theory,[56] for an eigenmode induced by an antenna, its saturated intensity is given by

$$A^2 \propto \frac{1}{(\omega_0^2 + \gamma^2 - \omega_{ant}^2)^2 + 4\gamma^2\omega_{ant}^2}. \tag{19}$$

Here, A^2 is the normalized saturated intensity, ω_0 is the eigenfrequency, and γ is the damping rate. Figure 4(a) shows the numerical fit to Eq. (19) that is obtained for the simulation results from an antenna frequency scan of the saturated e-BAE amplitude. The eigenfrequency is $\omega = \pm 1.636 c_s/R_0$, and the damping rate is $\gamma = -0.415 c_s/R_0$. The fitted eigenfrequency is slightly higher than the accumulation point frequency, $\omega_{CAP} = 1.515 c_s/R_0$, which may be due to the kinetic effects of the thermal ions together with the assumption of a small ϵ. When we set $\omega_{ant} = 1.6362 c_s/R_0$, as shown in Fig. 4(b), the mode amplitude saturates quickly, after approximately four oscillations, because of the large damping rate. The mode structure is still symmetric in the radial direction, and it is localized in space, as shown in Fig. 4(c).

B. BAE simulation with an initial perturbation

In the initial perturbation simulation, we first consider an external antenna that imposes a harmonic of $n/m=1/3$ as a $\delta\phi$ perturbation at the $q=3$ rational surface to excite the BAE. Then, the external antenna, which has a frequency of $\omega_{ant} = 1.515 C_s/R_0$, is turned off at time $= 5C_s/R_0$. In this scenario, the system is dominated by the BAE and shows an initial perturbation decay after the antenna is turned off. Two fluid equations are used to describe the system; ion Landau damping and other kinetic effects from particles are dropped. The time evolution of the $n/m=1/3$ mode is shown in Fig. 5(a), where the dotted line indicates the antenna-driven part, which serves as the initial perturbation, and the solid line represents the decay part after the antenna is turned off. $\delta\phi$ decays rapidly (the solid line) in the initial perturbation case, and the mode has $\omega = \pm 1.6968 c_s/R_0$; this is slightly higher than the accumulation point frequency, which may be due to the measurement error associated with the abrupt and rapid decay. The background noise is not negligible when the amplitude is low. The damping rate is $\gamma = -0.894 c_s/R_0$, which is due to the fact that the eigenfrequency is very close to the accumulation point of the continuous spectrum, so the continuum damping is strong. The mode structure is shown in Fig. 5(b); no phase mixing is observed in the region, and the mode is radially localized and symmetric.

A similar scenario is considered to investigate the influence of the thermal particle pressure gradient on the mode. In the following case, the linear Vlasov equation is used to describe the thermal ions, and the electrons are treated adiabatically. Figure 6 shows the time evolution of the $n/m=1/3$ mode with (red line) and without (black line) a pressure gradient of the thermal particles. Here, the antenna is turned off

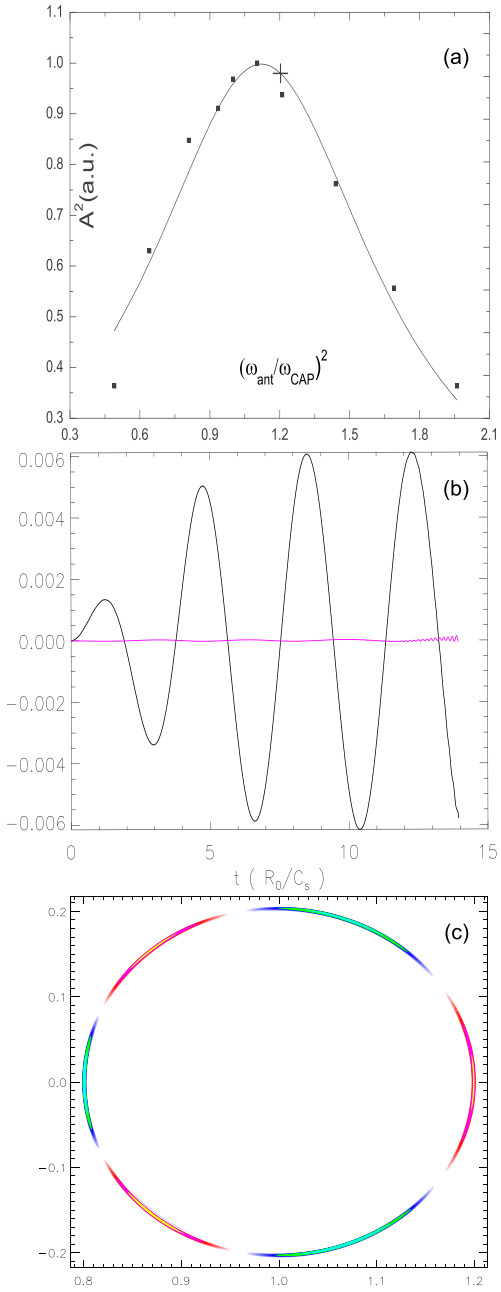

FIG. 4. (a) Saturated amplitudes at different antenna driving frequencies. The line is the numerical fit obtained using $A^2 \propto 1/((\omega_0^2+\gamma^2-\omega_{ant}^2)^2+4\gamma^2\omega_{ant}^2)$. The eigenfrequency is $\omega = 1.08\omega_{CAP}$, and the corresponding damping rate is $\gamma = -0.41\omega_{cap}$. The plus sign marks the eigenfrequency. (b) Time evolution of $\delta\phi$ when $\omega_{ant} = 1.08\omega_{CAP}$. (c) Poloidal mode structure of $\delta\phi$ excited by an antenna.

at the maximum value of $\delta\phi$, and the thermal particle pressure gradient is maintained during the antenna-driven part in both cases to ensure the same initial conditions. Then, the curves on the right side of the vertical line represent the decay after the antenna is turned off, and the black curve represents the case in which the thermal particle

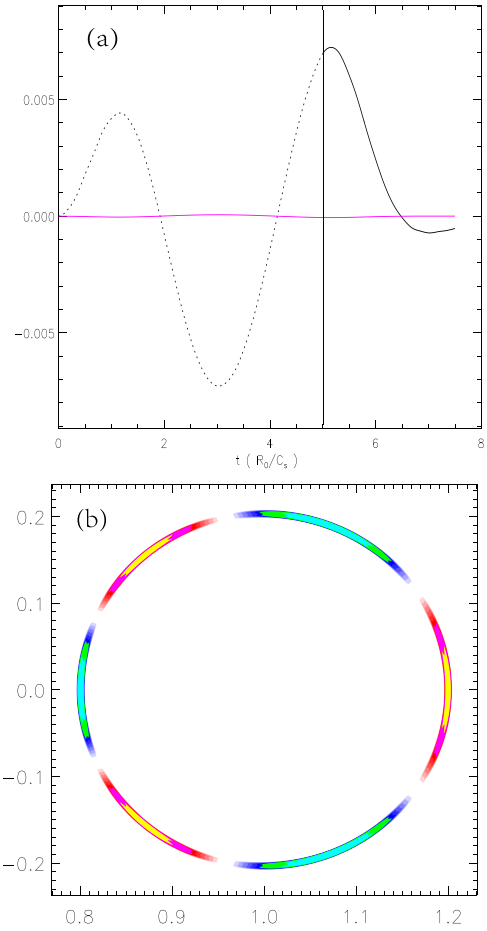

FIG. 5. (a) Time history of the electrostatic potential $\delta\phi$ with an initial perturbation. The dotted curve represents the antenna-driven part, and the solid curve represents the decay after the antenna is turned off. The eigenfrequency is $\omega = \pm 1.697 C_s/R_0$, and the corresponding damping rate is $\gamma = -0.894 C_s/R_0$. (b) Poloidal mode structure of the electrostatic potential $\delta\phi$ with an initial perturbation.

pressure gradient is set to zero. Corresponding to the red curve, the eigenfrequency with the thermal particle pressure gradient is $\omega = \pm 1.693 C_s/R_0$, and the damping rate is $\gamma = -0.265 c_s/R_0$. The eigenfrequency is almost the same as in the antenna-driven case because the same physical model is used to describe the particles in both cases, while the damping rate is slightly smaller compared to the antenna-driven case due to the judgment of the saturation point and the numerical error caused by an insufficient wave number. Corresponding to the black curve, the eigenfrequency without the thermal particle pressure gradient is $\omega = \pm 1.683 C_s/R_0$, and the damping rate is $\gamma = -0.255 c_s/R_0$. We can see that the pressure gradient of the thermal particles has a slight inhibitory effect on the excitation of the BAE.

C. BAE excitation by energetic electrons

In the low-β discharge, we use a temperature gradient of the energetic electrons to excite the e-BAE. In our work, a typical energetic electron temperature profile is expressed as follows:

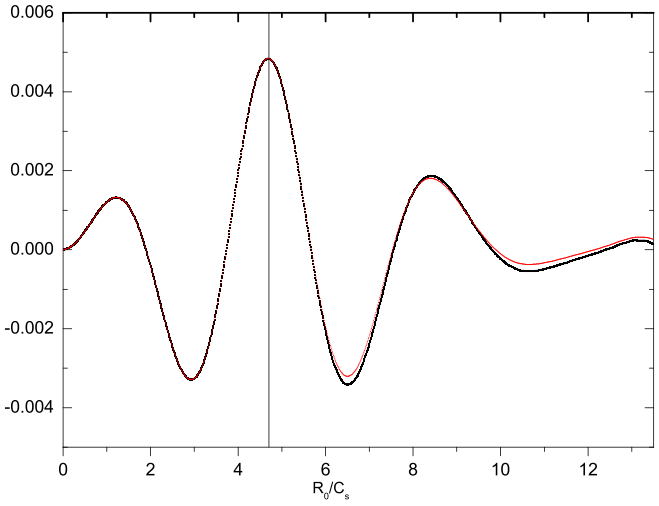

FIG. 6. Time history of the electrostatic potential $\delta\phi$ with an initial perturbation. The curve on the left side of the vertical line represents the antenna-driven part; here, a pressure gradient of the thermal particles is maintained in both cases. The curves on the right side of the vertical line represent the decay after the antenna is turned off. For the red curve, the thermal particle pressure gradient is maintained; the eigenfrequency is $\omega = \pm 1.693 C_s/R_0$, and the corresponding damping rate is $\gamma = -0.265 C_s/R_0$. For the black curve, the thermal particle pressure gradient is set to zero; the eigenfrequency is $\omega = \pm 1.683 C_s/R_0$, and the corresponding damping rate is $\gamma = -0.255 C_s/R_0$.

$$T_{fe} = 14.5 \times \{1.0 + 0.45[\tanh(0.83 - \rho)/0.01] - 1\} T_e. \quad (20)$$

The energetic electrons' temperature gradient reaches its maximum at $\rho = 0.83$ near the $q = 3$ rational surface with $R_0/L_{T_{fe}} = 180$, where $L_{T_{fe}}$ is the scale length of the temperature gradient; the density gradient of the energetic electrons is not considered in this work. The energetic electrons have an on-axis density of $n_{fe} = 0.25 n_e$ and an on-axis temperature of $T_{fe} = 14.5 T_e$. The scale length of the background plasma's density gradient is $R_0/L_{n_e} = 5.9$, which is much smaller than that of the energetic electrons' temperature gradient.

In our particular simulation region, $0.696 \leqslant \rho \leqslant 0.952$, $k_\parallel = (nq - m)/Rq$ varies from 0.23 to -0.16, and $k_\perp = m/r$ varies from 10.79 to 7.89; thus, the general assumption that $k_\parallel \ll k_\perp$ in Eq. (1) is not violated in this low-n e-BAE simulation.

In these simulation scenarios, the e-BAE grows exponentially, and it does not saturate in the linear stage. The time evolution of $\delta\phi$ is shown in Fig. 7(a), where the x-axis is normalized with respect to C_s/R_0 and the y-axis represents $\delta\phi$. The frequency is $\omega = 1.653 C_s/R_0$, and $f = \omega/2\pi = 19.96$ kHz, with a growth rate of $\gamma = 0.447 C_s/R_0$. The eigenfrequency in the energetic-electron-driven case is very close to the eigenfrequencies in both the antenna-driven case and the initial perturbation case, and it is slightly higher than the experimental observation of $f_{observation} = 19$ kHz. The real part of the mode (black line) is $\pi/2$ ahead of the imaginary part, indicating that it is a traveling wave. As shown in Fig. 7(b), the eigenfrequency without a pressure gradient of the thermal particles is $\omega = 1.653 C_s/R_0$, and the corresponding damping rate is $\gamma = 0.467 c_s/R_0$. We can see that the thermal particle pressure gradient has a slight inhibitory effect on the excitation of the BAE; this behavior is the same as that in the initial perturbation case, which originates from radiative damping.

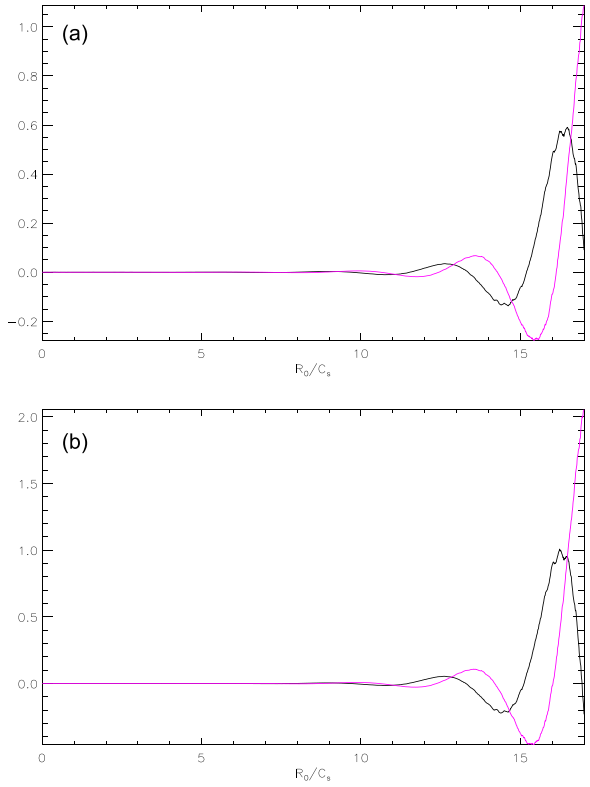

FIG. 7. (a) Time history of the electrostatic potential $\delta\phi$ for a BAE excited by energetic electrons with a thermal particle pressure gradient. The black and red lines represent the real and imaginary parts, respectively. The eigenfrequency is $\omega = 1.653 C_s/R_0$, and the corresponding damping rate is $\gamma = 0.447 C_s/R_0$. (b) Time history of the electrostatic potential $\delta\phi$ without a thermal particle pressure gradient. The eigenfrequency is $\omega = 1.653 C_s/R_0$, and the corresponding damping rate is $\gamma = 0.467 C_s/R_0$.

The accurate frequencies and damping/growth rates from the three simulations together with the frequencies corresponding to the experimental observation and the accumulation point are listed in Table I. Here, the e-BAE is destabilized by energetic electrons when the driving force of the energetic electrons exceeds the total background damping.

In addition, the radial symmetry of the e-BAE mode structure is broken, in contrast to the antenna-driven case; as shown in Fig. 8(a), the ellipse is twisted into a triangle. The kinetic effects of the energetic electrons give rise to the twisted mode structure.[57]

The polar structure of $\delta\phi$ rotates in the counterclockwise direction, and the magnetic field points out of the paper. From $\mathbf{v}_{D\alpha} = -\nabla P \times \mathbf{B}/(q_\alpha n_\alpha B^2)$, we can see that the mode propagates along the diamagnetic direction of the energetic electrons. The mode is still sensitive to the peak where the gradient of the energetic electrons reaches its maximum; the largest growth rate is observed when the T_{fe} peak is left-shifted from the $q = 3$ rational surface by approximately $3.3\rho_{fe}$ in the radial direction. The peak-shift phenomenon may be due to the antisymmetry of the mode structure caused by the kinetic effect of the energetic electrons.

In a sheared magnetic field, the e-BAE is highly radially localized near the rational surface. The mode width is narrow in the radial

TABLE I. The accurate frequencies and damping/growth rates measured with respect to the sound speed for the above scenarios.

Unit: C_s/R_0	ω	γ
MHD accumulation point	1.515	
Antenna excitation (with kinetic ions)	±1.636	−0.415
Initial perturbation (no kinetic ions)	±1.697	−0.894
Initial perturbation (with a pressure gradient of thermal particles)	±1.693	−0.265
Initial perturbation (no pressure gradient of thermal particles)	±1.683	−0.255
Energetic-electron excitation (with a pressure gradient of thermal particles)	1.653	0.447
Energetic-electron excitation (no pressure gradient of thermal particles)	1.653	0.467
Experimental observation	1.575	

direction; here, the mode width is the full width at half maximum (FWHM) of the $\delta\phi$ of the dominant $n/m = 1/3$ harmonic. The mode width can be obtained through Fourier analysis of $\delta\phi$, and the corresponding analysis results are shown in Fig. 8(b), where the x-axis is normalized with respect to r/a and the y-axis is normalized with respect to the maximum of $\delta\phi$.

No obvious balloon structure is observed in the linear stage because the $m = 2, 4$ harmonics are weak compared to the $m = 3$ harmonic, as shown in Fig. 8(b), meaning that the different harmonics do not obviously couple. Figures 8(c) and 8(e) show the poloidal structures of the vector potential $\delta A_\parallel$ and the effective potential $\delta\phi_{eff}$ of the mode at approximately 15 C_s/R_0. Figures 8(d) and 8(f) show the corresponding radial profiles for various harmonics. The $m = 4$, 2 sideband is much smaller than the dominant harmonic $m = 3$ for $\delta\phi$. The $m = 3$ harmonic of $\delta A_\parallel$ at the $q = 3$ rational surface is 0 because $k_\parallel \simeq 0$ for the main harmonic. $\delta\phi_{eff}$ is much smaller than $\delta\phi$, and the sideband is comparable to the harmonics, indicating that the sideband is likely to enhance the amplitude of the e-BAE.

For further study, convergence tests were conducted for the case of e-BAE excitation by energetic electrons. As the density of the background thermal electrons increases, the frequency shifts slightly downward, and the growth rate greatly increases, as shown in Fig. 9(a). At the same time, the mode width increases (although the mode remains localized) as β increases (implying a density change) as shown in Fig. 9(b). A scan of the energetic electron density n_{fe} shows that as n_{fe} increases, the growth rate also increases, but the e-BAE frequency barely changes, as seen in Fig. 9(c). A scan of the energetic electron

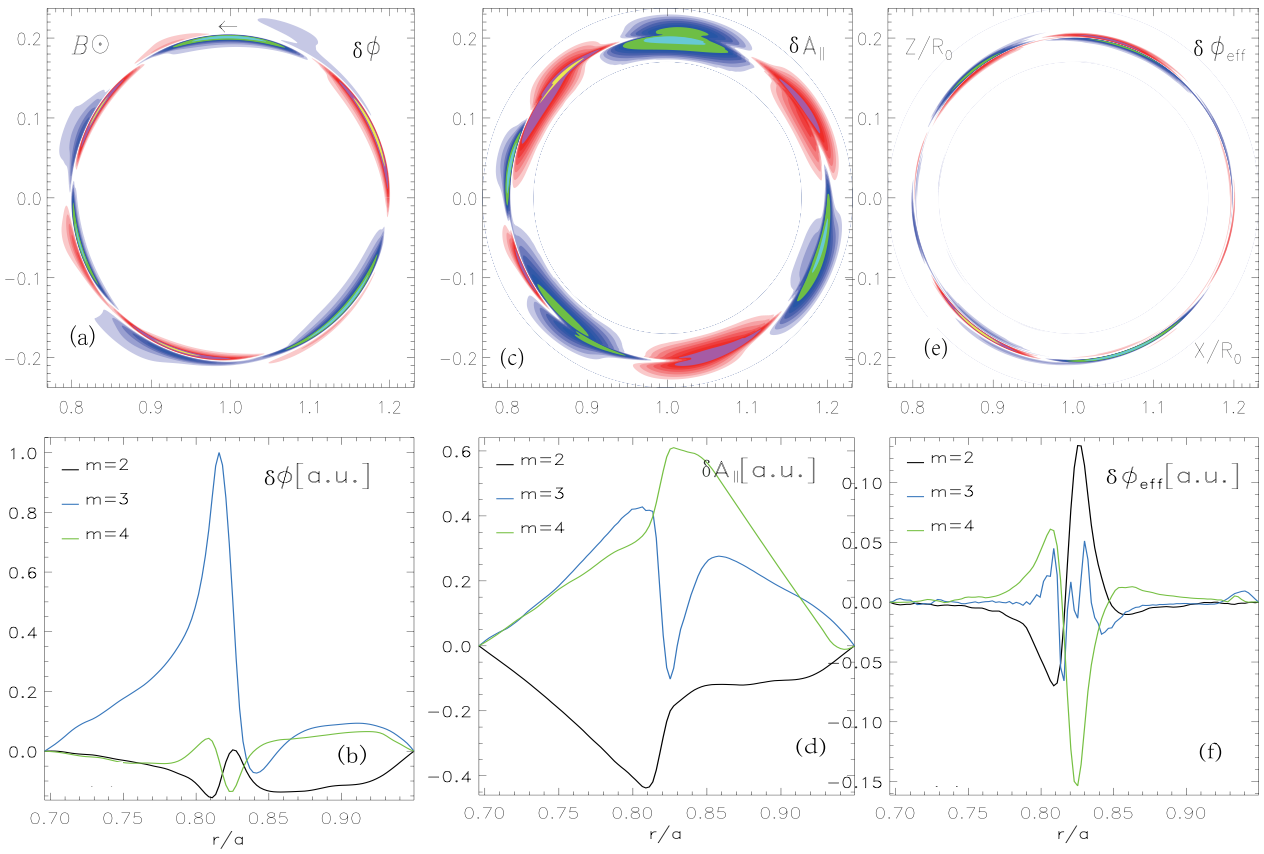

FIG. 8. (a), (c), and (e) Poloidal mode structures and (b), (d), and (f) radial profiles of the electrostatic potential $\delta\phi$, the vector potential $\delta A_\parallel$, and the effective potential $\delta\phi_{eff}$ for the main harmonic and other harmonics (with various values of m). All are normalized with respect to the maximum value of $\delta\phi$.

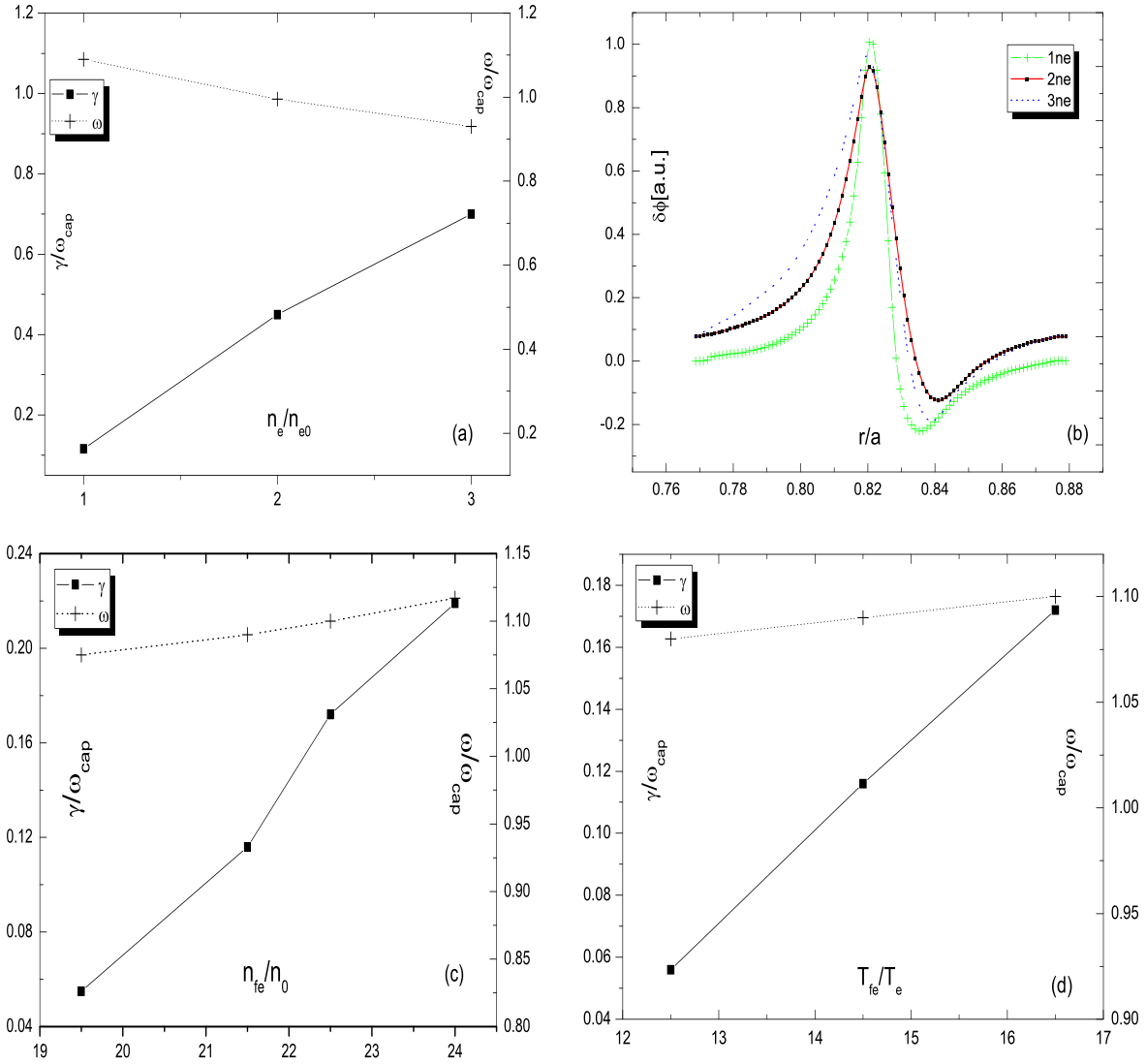

FIG. 9. (a) Scan of the background density n_e when $T_{fe} = 14.5$ and $n_{fe} = 0.25$ for the e-BAE frequency and a linear growth rate. (b) Radial profiles of ϕ at different n_e values, all normalized with respect to their own maxima. (c) and (d) Scans of (c) the energetic electron density n_{fe} when $T_{fe} = 14.5$ and (d) the energetic electron density T_{fe} when $n_{fe} = 0.2$ for the e-BAE frequency and a linear growth rate. The linear relationship is $\gamma/\omega_{CAP} = -0.305 + 0.029T_{fe}/T_e$. The value at the intercept of the growth rate divided by the frequency is -0.305, and the damping rate is $-0.305\omega_{CAP} = -0.462c_s/R_0$, which is close to that in the antenna excitation case.

temperature T_{fe} shows that as T_{fe} increases, the frequency changes slightly, but the growth rate increases greatly, as seen in Fig. 9(d). In the T_{fe} scan, T_{fe} and γ show a nearly linear dependence; the linear relationship is $\gamma/\omega_{CAP} = -0.4666 + 0.04T_{fe}/T_e$. The value at the intercept of the growth rate divided by the frequency is -0.47, and the damping rate is $-0.466\omega_{CAP} = -0.71c_s/R_0$, which is close to the value in the antenna-driven case.

D. Discussion

For low-frequency waves, the wave-particle resonance condition for deeply trapped particles is $\omega - \omega_d - p\omega_b = 0$. Further analysis reveals only the precessional resonance of trapped energetic electrons,[28] where the precession frequency is proportional to the toroidal mode number. At the same time, the driving force from the precession should overcome Landau damping,[58] continuum damping,[59,60] radiative damping,[61] and so on when the e-BAE is excited. In balance, the most unstable behavior is observed only in a certain range of mode numbers.[6] In our work, in simulation setups that are identical except for the mode number, higher-n modes such as $n/m = 2/6$ have not been driven, indicating that the $n/m = 1/3$ mode is the most unstable mode under these parameters, in good agreement with the experimental observation.

When we include the collision term, the frequency remains almost unchanged, and the growth rate shifts downward by approximately 4.5%, indicating that collisions between particles barely

TABLE II. The eigenfrequencies for multimode e-BAEs ($n/m = 1/2$, $n/m = 2/5$, and $n/m = 1/3$) measured at the MHD accumulation point, as experimentally observed and simulated (driven by energetic electrons) for HL-2A discharge #17929 (900 ms).

17929 (900 ms)	$n/m = 1/2$	$n/m = 2/5$	$n/m = 1/3$
ω_{CAP}	0.275 C_s/R_0	0.275 C_s/R_0	0.275 C_s/R_0
f_{CAP}	28 kHz	20 kHz	14.43 kHz
f_{exp}	24 kHz	17 kHz	12 kHz
ω_{ep}	$0.28875C_s/R0$	$0.3125C_s/R0$	$0.2875C_s/R0$
f_{ep}	29.4 kHz	22.7 kHz	15.01 kHz

influence the excitation of the e-BAE in this linear simulation. The reason is that the collision rates are $\nu_{ei} = 2.41$ kHz and $\nu_{ee} = 4.83$ kHz, which are much lower than the mode frequency. Here, we use $\nu_{\alpha\beta} = (\pi n_\beta q_\alpha^2 q_\beta^2)/((4\pi\epsilon_0)^2 m_\alpha^{1/2} T_\alpha^{3/2}) \ln\Lambda(\alpha = e, \beta = e, i)$ to estimate the collision rates, where $\ln\Lambda$ is the Coulomb logarithm and is approximately constant.

The coexistence of e-BAEs with different mode numbers ($n/m = 1/2$, $n/m = 2/5$, and $n/m = 1/3$) was observed in discharge #17 929 at 900 ms.[24] Based on the realistic experimental discharge parameters and profiles, three separate corresponding simulations have been conducted. For all three simulations, the physical model is the same as that for the energetic-electron-driven case in this manuscript, with the energetic electron profile adjusted as appropriate for each individual case. The eigenfrequencies for the different modes are shown in Table II for comparison with the experimental results. Further nonlinear simulations and analysis should still be performed to study multimode e-BAE phenomena.

V. SUMMARY AND FUTURE WORK

In this work, using the basic safety factor profile, temperature profile, and density profile from shot #17461 in the HL-2A tokamak at approximately 575 ms, the excitation of an e-BAE by a temperature gradient of the energetic electrons was successfully simulated with GTC. In our simulations, the real e-BAE frequencies measured in simulations with an initial perturbation, an antenna excitation, and an energetic electron excitation were almost the same as the experimental observation. The kinetic effects of the thermal ions and energetic electrons together excite the e-BAE, while the eigenfrequency is not greatly affected; moreover, the kinetic effect of the energetic electrons breaks the symmetry of the mode structure. The continuum damping is responsible for the large damping rate in the initial perturbation case. The radiative damping is responsible for the differences in damping rate between the cases with and without a pressure gradient of the thermal particles. The e-BAE propagates along the diamagnetic direction of the electrons. Its most unstable mode number is $n/m = 1/3$, which is consistent with the experimental observation. As the background β increases, the mode width also increases, and the frequency shifts downward. The growth rate strongly depends on the density and temperature profiles of the energetic electrons; moreover, a pressure gradient of the thermal particles has a slight inhibitory effect on the excitation of the BAE.

Under real experimental conditions, the energetic electrons are more likely to have a slowing down distribution instead of the Maxwell distribution used in our simulations. Therefore, our next goal is to use a slowing down distribution to induce an e-BAE, which may decrease the energetic electron density to a more reasonable level.

A multimode phenomenon was also experimentally observed in HL-2A shot #17929. However, no obvious mode coupling was seen in the experiment. Coupling between different modes, specifically with different n values, in the nonlinear stage will be the focus of our future work.

ACKNOWLEDGMENTS

The authors gratefully acknowledge useful discussions with Dr. W. Chen, L. Yu, H. Zhang, and J. Cao. This work was supported by the National MCF Energy R&D Program under Grant Nos. 2018YFE0304100, 2018YFE0311300, and 2017YFE0301300, the National Natural Science Foundation of China under Grant Nos. 11835016, 11675257, 11675256, 11875067, and 11705275, the Strategic Priority Research Program of the Chinese Academy of Sciences under Grant No. XDB16010300, the Key Research Program of Frontier Science of the Chinese Academy of Sciences under Grant No. QYZDJ-SSW-SYS016, and the External Cooperation Program of the Chinese Academy of Sciences under Grant No. 112111KYSB20160039. Resources used in this research were provided by the National Supercomputing Center of Tianjin (NSCC-TJ), the Oak Ridge Leadership Computing Facility at Oak Ridge National Laboratory (OLCF), and the National Energy Research Scientific Computing Center (NERSC).

REFERENCES

[1]See also, http://www.iter.org, for information about for "ITER 1988."
[2]C. Z. Cheng, L. Chen, and M. S. Chance, Ann. Phys. **161**, 21 (1985).
[3]H. Kimura, Y. Kusama, M. Saigusa, G. Kramer, K. Tobita, M. Nemoto, T. Kondoh, T. Nishitani, O. D. Costa, T. Ozeki *et al.*, Nucl. Fusion **38**, 1303 (1998).
[4]M. S. Chu, J. M. Greene, L. L. Lao, A. D. Turnbull, and M. S. Chance, Phys. Fluids B **4**, 3713 (1992).
[5]F. Zonca, L. Chen, and R. A. Santoro, Plasma Phys. Controlled Fusion **38**, 2011 (1996).
[6]A. D. Turnbull, E. J. Strait, W. W. Heidbrink, M. S. Chu, H. H. Duong, J. M. Greene, L. L. Lao, T. S. Taylor, and S. J. Thompson, Phys. Fluids B **5**, 2546 (1993).
[7]S. Tsai and L. Chen, Phys. Fluids B **5**, 3284 (1993).
[8]S. Briguglio, C. Kar, F. Romanelli, G. Vlad, and F. Zonca, Plasma Phys. Controlled Fusion **37**, A279 (1995).
[9]C. Cheng, N. Gorelenkov, and C. Hsu, Nucl. Fusion **35**, 1639 (1995).
[10]R. A. Santoro and L. Chen, Phys. Plasmas **3**, 2349 (1996).
[11]N. Gorelenkov and W. Heidbrink, Nucl. Fusion **42**, 150 (2002).
[12]W. W. Heidbrink, E. J. Strait, M. S. Chu, and A. D. Turnbull, Phys. Rev. Lett. **71**, 855 (1993).
[13]R. Nazikian, Z. Chang, E. D. Fredrickson, E. Mazzucato, S. H. Batha, R. Bell, R. Budny, C. E. Bush, C. Z. Cheng, and A. Janos, Phys. Plasmas **3**, 593 (1995).
[14]M. J. Hole, C. M. Ryu, M. H. Woo, J. G. Bak, S. E. Sharapov, M. Fitzgerald, and T. K. Team, Plasma Phys. Controlled Fusion **55**, 045004 (2013).
[15]C. Nguyen, X. Garbet, R. Sabot, L. G. Eriksson, M. Goniche, P. Maget, V. Basiuk, J. Decker, D. Elbze, and G. T. A. Huysmans, Plasma Phys. Controlled Fusion **51**, 095002 (2009).
[16]P. Buratti, P. Smeulders, F. Zonca, S. Annibaldi, M. D. Benedetti, H. Kroegler, G. Regnoli, O. Tudisco, and the FTU-team, Nucl. Fusion **45**, 1446 (2005).
[17]S. Okada, M. Inomoto, S. Yamamoto, T. Masumoto, S. Yoshimura, and K. Kitano, Nucl. Fusion **47**, 677 (2007).
[18]M. Xu, W. Chen, L. Q. Hu, R. J. Zhou, G. Q. Zhong, T. H. Shi, L. Q. Xu, Y. Zhang, Y. W. Sun, S. Y. Lin *et al.*, Plasma Phys. Controlled Fusion **55**, 065002 (2013).
[19]H. R. Koslowski, E. Westerhof, M. De Bock, I. Classen, R. Jaspers, Y. Kikuchi, A. Krämerflecken, A. Lazaros, Y. Liang, and K. Löwenbrück, Plasma Phys. Controlled Fusion **48**, B53 (2006).

[20]A. Fasoli, C. Gormenzano, H. Berk, B. Breizman, S. Briguglio, D. Darrow, N. Gorelenkov, W. Heidbrink, A. Jaun, S. Konovalov *et al.*, Nucl. Fusion **47**, S264 (2007).
[21]L. Chen and F. Zonca, Nucl. Fusion **47**, S727 (2007).
[22]W. Chen, X. T. Ding, Q. W. Yang, Y. Liu, X. Q. Ji, Y. P. Zhang, J. Zhou, G. L. Yuan, H. J. Sun, and W. Li, Phys. Rev. Lett. **105**, 185004 (2010).
[23]Q. Yang, Y. Liu, X. Ding, J. Dong, L. Yan, D. Liu, W. Xuan, L. Chen, J. Rao, X. Duan *et al.*, Nucl. Fusion **47**, S635 (2007).
[24]X. Ding, W. Chen, L. Yu, S. Chen, J. Dong, X. Ji, Z. Shi, Y. Zhou, Y. Dong, X. Huang *et al.*, Nucl. Fusion **53**, 043015 (2013).
[25]W. Chen, X. T. Ding, Y. Liu, Q. W. Yang, X. Q. Ji, G. L. Yuan, Y. P. Zhang, M. Isobe, Y. B. Dong, and Y. Huang, Nucl. Fusion **51**, 063010 (2011).
[26]L. Liu, J. He, Q. Hu, and Z. Ge, Plasma Phys. Controlled Fusion **57**, 65007 (2015).
[27]L. Chen and F. Zonca, Phys. Plasmas **24**, 072511 (2017).
[28]J. Cheng, W. Zhang, Z. Lin, I. Holod, D. Li, Y. Chen, and J. Cao, Phys. Plasmas **23**, 052504 (2016).
[29]J. Cheng, W. Zhang, Z. Lin, L. Ding, D. Chao, and J. Cao, Phys. Plasmas **24**, 092516 (2017).
[30]Z. Lin, T. S. Hahm, W. W. Lee, W. M. Tang, and R. B. White, Science **281**, 1835 (1998).
[31]W. Zhang, I. Holod, Z. Lin, and Y. Xiao, Phys. Plasmas **19**, 022507 (2012).
[32]C. Zhang, W. Zhang, Z. Lin, and D. Li, Phys. Plasmas **20**, 052501 (2013).
[33]Z. Wang, Z. Lin, I. Holod, W. W. Heidbrink, B. Tobias, Z. M. Van, and M. E. Austin, Phys. Rev. Lett. **111**, 145003 (2013).
[34]W. Deng, Z. Lin, and I. Holod, Nucl. Fusion **52**, 023005 (2012).
[35]W. Deng, Z. Lin, I. Holod, Z. Wang, Y. Xiao, and H. Zhang, Nucl. Fusion **52**, 043006 (2012).
[36]H. S. Zhang, Z. Lin, I. Holod, X. Wang, Y. Xiao, and W. L. Zhang, Phys. Plasmas **17**, 112505 (2010).
[37]H. S. Zhang, Z. Lin, and I. Holod, Phys. Rev. Lett. **109**, 025001 (2012).
[38]Y. Liu, Z. Lin, H. Zhang, and W. Zhang, Nucl. Fusion **57**, 114001 (2017).
[39]X. Wang, F. Zonca, and L. Chen, Plasma Phys. Controlled Fusion **52**, 115005 (2010).
[40]X. Wang, S. Briguglio, L. Chen, T. C. Di, G. Fogaccia, G. Vlad, and F. Zonca, Phys. Rev. E **86**, 045401 (2012).
[41]S. Briguglio, F. Zonca, and G. Vlad, Phys. Plasmas **5**, 3287 (1998).
[42]X. Wang, S. Briguglio, L. Chen, C. D. Troia, G. Fogaccia, G. Vlad, and F. Zonca, Phys. Plasmas **18**, 052504 (2011).
[43]W. Park, J. Breslau, J. Chen, G. Fu, S. Jardin, S. Klasky, J. Menard, A. Pletzer, B. Stratton, D. Stutman *et al.*, Nucl. Fusion **43**, 483 (2003).
[44]W. Park, E. V. Belova, G. Y. Fu, X. Z. Tang, H. R. Strauss, and L. E. Sugiyama, Phys. Plasmas **6**, 1796 (2000).
[45]Z.-Z. Ren, G. Y. Fu, M. A. Van Zeeland, F. Wang, Z.-X. Wang, R. Nazikian, F. Turco, and C. C. Petty, Phys. Plasmas **25**, 122504 (2018).
[46]H. Rizvi, A. Panwar, M. Shahzad, and C. M. Ryu, Plasma Phys. **23**, 122515 (2016).
[47]H. S. Xie and X. Yong, Phys. Plasmas **22**, 022518 (2015).
[48]A. J. Brizard and T. S. Hahm, Rev. Mod. Phys. **79**, 421 (2007).
[49]I. Holod, W. L. Zhang, Y. Xiao, and Z. Lin, Phys. Plasmas **16**, 122307 (2009).
[50]Z. Lin and W. W. Lee, Phys. Rev. E **26**, 5646 (1995).
[51]A. Smolyakov, C. Nguyen, and X. Garbet, Nucl. Fusion **50**, 054002 (2010).
[52]A. Mishchenko, A. Könies, and R. Hatzky, Phys. Plasmas **16**, 082105 (2009).
[53]W. Deng, Z. Lin, I. Holod, X. Wang, Y. Xiao, and W. Zhang, Phys. Plasmas **17**, 112504 (2010).
[54]A. Fasoli, D. Borba, G. Bosia, D. J. Campbell, J. A. Dobbing, C. Gormezano, J. Jacquinot, P. Lavanchy, J. B. Lister, P. Marmillod *et al.*, Phys. Rev. Lett. **75**, 645 (1995).
[55]A. Fasoli, D. Testa, T. Panis, A. Klein, J. A. Snipes, J. Sears, M. Gryaznevich, R. Martin, S. D. Pinches, and J-E Contributors, Plasma Phys. Controlled Fusion **52**, 075015 (2010).
[56]W. Benenson, J. W. Harris, H. Stocker, and H. Lutz, *Handbook of Physics* (Springer-Verlag Inc, 2002).
[57]R. Ma, F. Zonca, and L. Chen, Phys. Plasmas **22**, 092501 (2015).
[58]R. Betti and J. P. Freidberg, Phys. Fluids B **4**, 1465 (1992).
[59]M. N. Rosenbluth, H. L. Berk, J. W. Van Dam, and D. M. Lindberg, Phys. Rev. Lett. **68**, 596 (1992).
[60]F. Zonca and L. Chen, Phys. Rev. Lett. **68**, 592 (1992).
[61]R. R. Mett and S. M. Mahajan, Phys. Fluids B **4**, 2885 (1992).